JOURNAL OF PROPULSION AND POWER
Vol. 23, No. 1, January–February 2007

# Laser-Driven Decomposition and Combustion of BTTN/GAP

Jianquan Li* and Thomas A. Litzinger†
*Pennsylvania State University, University Park, Pennsylvania 16802*

DOI: 10.2514/1.20293

**The objective of this work was to study the near-surface phenomena of an energetic binder, butanetriol trinitrate/glycidyl azide polymer, during thermal decomposition and combustion. A triple quadrupole mass spectrometer with microprobe sampling was used to obtain gas-phase quantitative species from $CO_2$ laser-induced decomposition and laser-assisted combustion of the butanetriol trinitrate/glycidyl azide polymer sample. To get the species profile as a function of height from the surface, a linear positioner was used to move the sample towards the microprobe during sampling. Fine-wire thermocouples were used to get the surface temperature and gas-phase temperature profile in the primary flame zone. The experiments were conducted at a laser heat flux of 35 $W/cm^2$ and in both argon environment and ambient air conditions with varying pressures from 1.0 to 4.0 atm. The flame structure and burning event were recorded using a digital camcorder so that the burning rates at these pressures can also be determined.**

## Introduction

THE costs for developing advanced propellants and/or propellant ingredients are very high both in time and in financial resources. An a priori predictive capability is thus highly desirable. Such a capability has been evolving over the past several years, which uses detailed kinetic mechanisms to model the combustion of a wide spectrum of propellant ingredients [1,2]. To reduce the complexity in modeling, multidimensional diffusion flames of propellants like ammonium perchlorate with energetic or nonenergetic binders have been avoided in early stages of efforts. Instead, a homogeneous one-dimensional flame is sought to simplify the comparison of modeling results with experimental measurements. Nitramines, such as cyclotrimethylene trinitramine (RDX) and cyclotetramethylene tetranitramine (HMX), do not have strong diffusion flames with various binders, and so two propellants containing the monopropellant RDX or HMX were selected for model development and validation, which are RDX/GAP/BTTN (glycidyl azide polymer/butanetriol trinitrate) and HMX/GAP/BTTN.

GAP is an energetic azide polymer; as shown in Fig. 1, it is very fuel rich. Because RDX and HMX are both stoichiometrically balanced, the mixtures of RDX/GAP and HMX/GAP are also fuel rich, resulting in lower burning rates and carbonaceous combustion residue. The addition of BTTN, a highly oxygenated energetic plasticizer, provides more oxygen and thus reduces char formation. The structure of BTTN is also shown in Fig. 1.

Critical to success in the modeling efforts are parallel experimental measurements, which are required for validation and refinement of the modeling codes. Experimental studies have been conducted on RDX/GAP/BTTN [3,4] and HMX/GAP/BTTN [5], and separately on RDX [6–8], HMX [8–10], BTTN [11–13] and GAP [14–21], but data on butanetriol trinitrate/glycidyl azide polymer (BTTN/GAP) is very limited. The only work on BTTN/GAP available in the literature is that of Roos and Brill [4]. In their work, a cured mixture of BTTN/GAP by weight of 70/30 was studied through *T*-jump/FTIR (Fourier transform infrared) spectroscopic measurements for pyrolysis products by flash heating at 450°C in 0.5 MPa argon. Their results showed that the flash pyrolysis of BTTN/GAP produces IR and Raman spectra that closely resemble that of BTTN alone, but no $NO_2$ or BTTN vapor was detected. The lack of $NO_2$ in BTTN/GAP was attributed to the completion of the reaction of $NO_2$ with the fuel fragments of GAP to form NO. Quantitative species data were presented in their results, but profiling the species was not available. Parr and Hanson-Parr used various spectroscopic techniques to measure species profiles point-by-point from a number of tests for the propellants RDX/GAP/BTTN [3] and HMX/GAP/BTTN.[5].

The reaction mechanism in the condensed phase remains a major challenge for the modelers; the near-surface species information would be helpful in determining a reaction mechanism for the condensed phase. The combustion behavior of BTTN/GAP would be critical to the understanding of the combustion of RDX/GAP/BTTN and HMX/GAP/BTTN and hence the model development. In the present work, the surface temperature and near-surface species of BTTN/GAP at a heat flux of 35 $W/cm^2$ were measured. Also, temperature and species profiles above the sample surface were obtained to map out the flame structure. The main technique used is tandem mass spectrometry, which is capable of differentiating species at the same mass and detecting species that are IR insensitive (e.g., $N_2$ and $H_2$) and thus cannot be detected by an FTIR spectrometer. The experimental results are expected to provide insight into the near-surface chemistry that would aid in determining the condensed-phase reaction mechanism, and to provide the modelers data for use in validation and improvement of their codes.

## Experimental

The experimental setup is schematically shown in Fig. 2. The main facilities include a heating source, a windowed test chamber, a linear positioner, a CCD camera and a video camcorder, as well as a triple quadrupole mass spectrometer (TQMS).

### Test Chamber

The test chamber is made of aluminum and is 25.4 cm tall and 16.5 cm on a side with 1.3 cm thick walls, giving an internal volume of 4, 460 $cm^3$, which is sufficiently large to maintain a constant ambient pressure in the chamber when a propellant sample is burning. A constant pressure is critical to determination of the effect of pressure on the burning rate. One side of the chamber interfaces with the sampling probe of the TQMS through specially designed flanges. Two high quality Plexiglas windows are installed on opposite sides of the chamber to allow video photography of the ignition and burning event. The video is acquired using a Sony camcorder and is used to examine the flame structure and as an aid in calculating the burning rate. In addition, a Pulnix video CCD camera equipped with a Nikon macro lens in conjunction with a TV screen is used to provide real-time monitoring of the test. A programmable linear

Presented as Paper 3765 at the 41st AIAA/ASME/SAE/ASEE Joint Propulsion Conference and Exhibit, Tucson, Arizona, 10–13 July 2005; received 28 September 2005; revision received 2 February 2006; accepted for publication 6 February 2006. 

*Postdoctoral Scholar, Department of Mechanical and Nuclear Engineering. Member AIAA.

†Professor, Department of Mechanical and Nuclear Engineering. Senior Member AIAA.

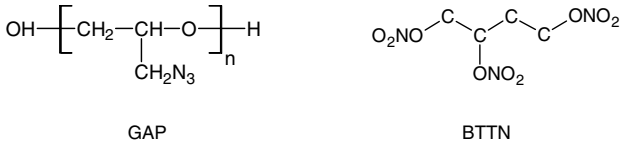


**Fig. 1 Molecular structures of GAP and BTTN.**

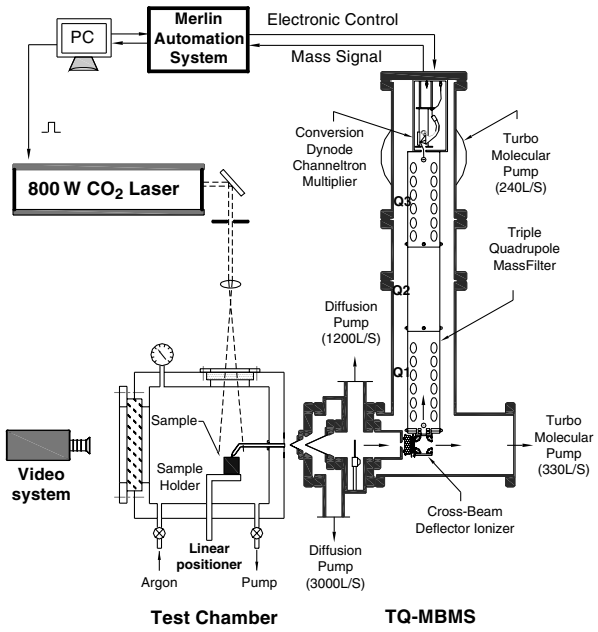


**Fig. 2 Schematic of experimental setup.**

positioner was attached to the center of the chamber bottom, and the shaft of the positioner enters the chamber and connects to a sample holder to provide precise control of vertical movement and positioning of the sample. During a test, the sample was pushed towards the sampling probe by the preprogrammed linear positioner to obtain species profiles. Several fittings and electrical feedthroughs were installed in the chamber walls to gain access to the chamber for purging and pressurizing the chamber with a desired background gas, evacuating the chamber by a vacuum pump, and sealing the passage of thermocouple signals out of the chamber.

The energy source for heating the samples was a high-power $CO_2$ laser with a maximum power output of 800 W in continuous wave mode. The laser beam passed through a collimating aperture (5 mm) and an expanding lens (zinc selenide) before entering the test chamber through a potassium chloride (KCl) window, which is 97% transmissive to the 10.6 $\mu$m laser beam. The size of the beam on the sample surface was selected to be about twice that of the sample surface so that a largely uniform beam profile could be achieved across the sample surface. Also, the large size of the beam was required when the sample is moving upwards to profile the gas-phase structure.

### Sample

The BTTN/GAP material was provided by the Naval Air Warfare Center (NAWC), China Lake, CA. The compositions of this material are, by weight, 80% BTTN plasticizer, 18.078% GAP polyol, 1.822% HMDI (hexamethyene diisocyanate) curative, and 0.1% T-12 (dibutyl tin dilaurate) catalyst. The cured BTTN/GAP is light brown in color and somewhat like a gel. The test samples were typically $5 \times 5 \times 8$ mm cut from a large block.

### Temperature Measurement

Surface temperature and near-surface gas-phase temperature profile were measured using thermocouples of chromel–alumel (type K) and platinum–platinum/13% rhodium (type R) with bead sizes of 25–50 $\mu$m In the surface temperature measurement, the thermocouple wires were stretched across the sample surface by hanging two weights of $\sim$6.6 g over the edge of the sample surface. By doing so, the wires were kept under tension to prevent any slack in the wires so that the bead position was maintained on the sample surface throughout a test. The thermocouple bead was placed at the center of the sample surface and the measured temperature is thought to represent the temperature at the whole surface [22]. The type R thermocouple was used to profile the flame because type K thermocouple is more easily broken due to the higher temperature in the flame. Before a test the thermocouple was imbedded into the sample with its bead 2 mm below the surface. Since the thermocouple was held in still, as the sample burned, the thermocouple first recorded the condensed-phase and then gas-phase temperature profiles.

Data acquisition and reduction were done using a program developed in LabView. To minimize the effect [23] of the laser heat flux on the measured temperature, the heating was halted right after the sample ignited. Correction of the measured temperature due to thermal lag and radiative loss was not performed because the error is negligible for the small bead of the thermocouples [20] and the relatively low temperatures near the sample surface.

### Species Measurement

The sampling and analysis of gaseous species were performed using a triple quadrupole molecular-beam mass spectrometer (TQ-MBMS). The TQMS system along with the molecular-beam method was fully discussed in [24,25]. As depicted in Fig. 2, the mass spectrometer can perform sampling in two different configurations: one using microprobes and the other using a cone-skimmer configuration. In microprobe sampling, two quartz probes were used. The primary probe has dimensions of 50 mm (length), 2 mm (ID), and 3.2 mm (OD); its front end is fabricated by pulling during torch heating to form a conical tip, which is then ground to open an orifice of about 30 $\mu$m in diameter. The secondary probe (not shown in Fig. 2) is 120 mm (length), 4 mm (ID), and 6.35 mm (OD). The orifice of the secondary probe is about 100 $\mu$m, which is placed behind the primary probe with a gap of $\sim$1.0 mm. The advantages of the microprobe sampling are better spatial resolution and greater strength to take higher pressures in the test chamber. In the cone-skimmer scheme (the primary microprobe shown in Fig. 2 will be removed), a cone-shaped sampler is used, which is 20 mm long and has an orifice of 100 $\mu$m at its apex. The selection of relatively large included angles (interior 50 deg and exterior 55 deg) is expected to allow a "free" expansion for the supersonic jet developing inside. The skimmer is comparatively large both in length (50 mm) and in orifice diameter (1.5 mm), and has a 55 deg interior angle and a 60 deg exterior angle. Both the sampling cone and the skimmer were obtained from Beam Dynamics, Inc. A plating technique is employed to fabricate them using nickel. While maintaining the very sharp tips ($\sim$5 $\mu$m), double thickness of wall and additional rhodium plating were applied for improved mechanical strength and better protection from corrosion. Specially designed fixtures were used to hold the cone and the skimmer in place onto standard flanges for mounting to the vacuum chambers. The cone-skimmer distance is adjustable by using spacers for better beam performance. The use of cone-skimmer scheme enables molecular-beam sampling to directly probe unstable intermediate species such as radicals and ions.

Compared with molecular-beam sampling, microprobe sampling provides better spatial resolution and an angled probe tip can be easily realized for profiling species across the combustion wave, so that it was used throughout this work where emphasis was on the information of species near the surface region. However, the longer flight time of the sampled species in the microprobe and greater chances for collision among the species and with the probe walls raised concerns about dissociation and recombination that take place in the probe and affect the accuracy of the measured data. Lee et al. [26] performed a calculation to evaluate the gas-phase reaction in the probe and found that, under most severe conditions (1 torr and 1600 K in the probe), the maximum change for the most reactive species ($NO_2$) was about 5%. Reactions on the probe inner wall have

been reported to involve CO oxidation to $CO_2$, NO oxidation to $NO_2$, and dissociation of $NO_2$ to NO. However, they can be neglected due to the vacuum condition in the probe for CO to $CO_2$ [27] and due to the canceling effects in the relevant reactions for NO and $NO_2$ [28], that is, the equal chance for forming NO and $NO_2$. Therefore, it is thought reasonable to assume that such effects can be neglected.

The sample gases were drawn through the probe and into the mass spectrometer by two diffusion pumps and two turbomolecular pumps as well as their backing pumps forming a three-stage differential vacuum system ($10^{-3}/10^{-5}/10^{-7}$ torr) to meet the requirement imposed by the orifices. Ions are produced during electron impact in the ion region of an Extrel cross-beam-deflector ionizer, which is a combination of an axial ionizer mounted perpendicularly to the mass filter axis and a small quadrupole deflector energy filter. The energy-filtering capability of this ionizer provides great improvement in its sensitivity, because tuning the lenses of the energy filter can add energies up to hundreds of electron volts (eV) to the deflected beam. The right-angle configuration dramatically increases signal-to-noise by removing unwanted components of the sample, such as photons, energetic neutrals, and even particulates, because they are directly pumped away by the turbo pump behind the ionizer. This configuration also helps to reduce contamination of the quadrupoles and the detector for better performance in corrosive and high-particulate applications.

Two modes can be selected for the mass filtering operation of mass spectrometer: "parent" mode and "daughter" mode. Using the daughter mode of operation of the TQMS, it was possible to identify and differentiate $N_2$, CO, and, $C_2H_4$ with the same mass to charge ratio (m/z) at 28 amu (atomic mass unit, $1.660538 \times 10^{-27}$ kg), NO, $CH_2O$ at 30 amu, and $N_2O$, $CO_2$ at 44 amu. In the daughter mode, the ion of interest, often referred to as the parent, is selected in the first quadrupole (Q1). The parent ions then enter the second quadrupole (Q2) and are fragmented into smaller species, the daughters, by the process of collision-induced dissociation (CID) with an inert gas separately supplied into Q2. Argon was used as the collision gas in this study to minimize its contributions to fragmented species. The daughters, at masses less than their parent, are detected in the third quadrupole (Q3). For complex parent ions, some of the daughters might overlap if the parents contain common structures. In the present study, however, at least one unique daughter ion could be acquired for each parent ion.

Detection of the ions that pass through the mass filters was performed using a channeltron multiplier with a conversion dynode. An Extrel Merlin Automation system provides full electronic control of the TQMS system and performs data acquisition and reduction.

Several methods of calibration were used to obtain the sensitivity coefficients (intensity/concentration) of each species. The most stable species were calibrated directly with the gas mixtures of known concentration. To calibrate water, water vapor was acquired from liquid water that was vaporized by the $CO_2$ laser. Typically, the sensitivity factors were repeatable within 10%. The calibration factor of species for which standards were not readily available, for example, HCN, was estimated by correlating the signal intensity to that of calibrated species with a similar appearance potential through the ratio of their ionization cross sections [29].

For all the calibrations and in the actual tests, an ionization energy of 22 eV was used to minimize fragmentation of molecules and still get a sufficient number of ions to produce acceptable intensities. However, this setting was still high compared with the ionization energies of 9–15 eV for most organic compounds, thus, some fragments were formed and contributed to the signals at masses other than the parent mass. In such instances, these signals were subtracted from the mass signal of interest. Most of the species information will be reported as normalized mole fractions by totaling the measured concentrations of the sampled species and dividing each concentration by this total. The normalization eliminates the effect of sample temperature on the observed signal intensities because the temperature dependence cancels out. This method also cancels out the effect of probe orifice blockage during a test on signal intensity. To check if there are any major species missing during the sampling, element balances were performed through the reaction zones using the measured more fractions.

The sample holder was spring loaded with a weak spring and retained inside an outer guiding tube by a small sheet metal tab. The sample holder was mounted to the shaft top of the linear positioner. Before a test, the sample was arranged so that the probe tip is on the centerline of the sample at a distance of about 3 mm from the sample surface. The linear positioner was programmed at a speed of 2.5 mm/s. The spring-loaded sample holder allowed the sample to be driven up to and into the sampling probe without breaking the probe so that species profiles right down to the sample surface can be measured.

## Results and Discussion

### Observation of Event

In air at atmospheric pressure, the sample ignites at heat fluxes as low as 20 $W/cm^2$; after ignition, the laser heating is removed and sustained combustion is achieved. In 1 atm argon environment, ignition can also be achieved at 20 $W/cm^2$, but, unlike in air, self-sustained combustion cannot be achieved, so that the laser heating was kept on until completion of the combustion. To ensure ignition, a higher heat flux at 35 $W/cm^2$ was used for all tests in this work. Bright sparks were observed from the flames in both air and argon, which sometimes attached to the probe tip clogging the orifice.

Unlike the stable flame of BTTN, [11] the flame of BTTN/GAP is very unstable (especially in air), exhibiting an oscillatory behavior both in brightness and in size. It is believed that this oscillatory burning is attributed to the presence of GAP, as Saito et al. [20] observed a pulsating regression behavior of GAP. Figure 3 shows video images of the flame in 1 atm air.

Generally, the onset of a luminous flame was very abrupt, as shown in Fig. 3a, where the bright flame first observed suddenly rose to a distance about 15 mm above the surface. Then within 0.07 s, this flame touched down to the surface and spread out violently (observed from the video). As seen in the video image b), the spreading flame causes the side surfaces to burn. So, in tests to determine the burning rate, the side surfaces of the samples were coated with a layer of whiteout or "Liquid Paper" (containing titanium dioxide) in order to get a well-defined flame, as shown in Fig. 3c.

### Burning Rate

Experiments to determine the burning rate (here, defined as the rate at which the sample surface regresses with time) were conducted in air at pressures up to 4 atm with a laser heat flux of 35 $W/cm^2$ during which the surface temperature was simultaneously measured. As mentioned above, in order to prevent side-surface burning and also avoid thermocouple failure due to overheating by the side-spreading flame, the side surfaces of BTTN/GAP samples were precoated by a layer of Liquid Paper. However, in species measurements, the samples were not coated in order to reduce the chance of species contamination by the coating layer.

Figure 4 shows the results from this series of tests. As seen in Fig. 4, as pressure increases from 1 atm to 4 atm, the increase in surface temperature was not large, only about 10 K. However, the increase in the burning rate was large, from ~0.5 mm/s to ~1.4 mm/s.

a) b) c)

**Fig. 3 Video images of BTTN/GAP flame in 1 atm air: a) onset of ignition; b) sample side-surface without coating; c) sample side-surface coated with Liquid Paper.**

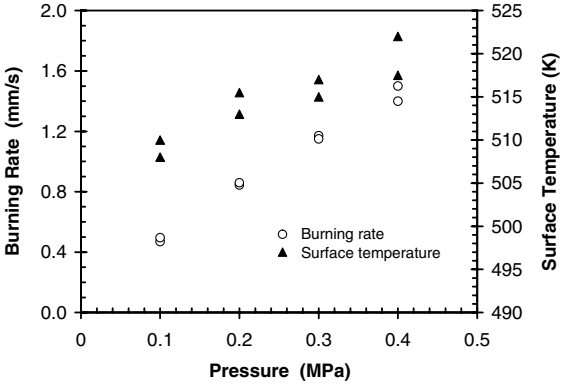


**Fig. 4 Burning rates and surface temperatures as functions of pressure during combustion of BTTN/GAP in air.**

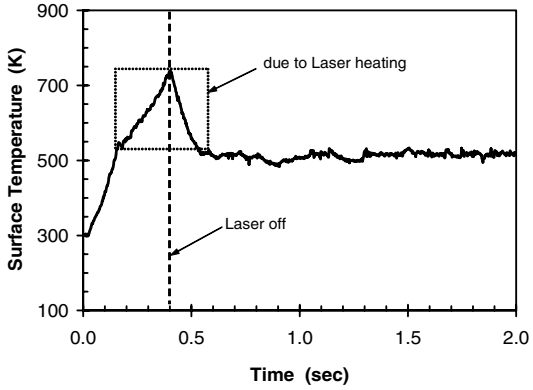


**Fig. 5 Surface temperature of BTTN/GAP during self-sustained combustion in 1 atm air.**

Compared with the burning rate of 0.5 mm/s of BTTN/GAP at atmospheric pressure in air, the pure liquid BTTN burns much slower, only 0.27 mm/s measured by Parr and Hanson-Parr [11]. Apparently, this difference is attributed to the presence of GAP. Korobeinichev et al. [21] measured the burning rates at the same pressure but in argon to be 18 mm/s and 10 mm/s for uncured and cured GAP, respectively, (the cured sample was preheated to 120°C, though). Tang et al. [19] determined the burning rate to be 6 and 10 mm/s for cured GAP samples during laser-assisted combustion in atmospheric air at heat fluxes of 100 and 200 W/cm$^2$, respectively.

### Surface Temperature

Figure 5 presents a typical result from surface temperature measurements, where the laser heating of 35 W/cm$^2$ was terminated at 0.4 s after triggering the laser as indicated in Fig. 5. The large spike (marked in the dotted square) in the curve is a combined effect of surface temperature and laser heating. After the laser heating was removed, the temperature at surface was determined to be about $510 \pm 6$ K at a pressure of 1 atm and the result was quite reproducible.

It is interesting to find that the surface temperature of BTTN/GAP is lower than those of both BTTN and GAP. From Parr and Hanson-Parr's result, the surface temperature for BTTN is 527 to 534 K [11]. For GAP, Tang et al. [19] claimed a surface temperature of 1050 K during laser-assisted combustion of cured GAP at atmospheric pressure with a heat flux of 100 W/cm$^2$, whereas Kubota and Sonobe [15] observed the temperature at surface to be ~700 K during self-sustained combustion at a pressure of 0.5 MPa (~5 atm). The large difference between their results is likely due to the laser heating effect in the work of Tang et al. [19] where the laser heating was not terminated until completion of the event. The lower surface temperature measured in this work suggests less heat feedback from the gas phase to the condensed phase and/or less production of heat of reaction in the condensed phase, where the decomposition products of BTTN and GAP may react with each other, adding complexity to the condensed-phase reaction mechanisms of BTTN or GAP alone. For BTTN and GAP mixed with RDX or HMX, the surface temperatures are 605 K for RDX/GAP/BTTN (~0.71/0.09/0.2 by weight) [3] and 785 K for HMX/GAP/BTTN ~0.71/0.09/0.2 by weight) [5], both much higher than that of BTTN/GAP alone.

### Temperature Profile

The temperature profile was obtained using 50 $\mu$m type R thermocouples, which were imbedded in the sample 2 mm below the surface. Figure 6 displays the measured temperature profile across the combustion wave of a BTTN/GAP sample with a height of 8 mm in atmospheric air. The zero height corresponds to the sample surface, at which the temperature was ~505 K in good agreement with the result from surface temperature measurements as shown in Fig. 5.

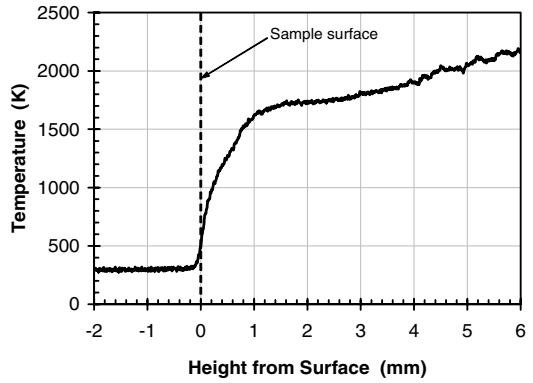


**Fig. 6 Temperature profile of BTTN/GAP during combustion in 1 atm air.**

The temperature rises rapidly to ~1650 K within a distance of about 1 mm from the surface, and then the increase becomes gradually from 1650 to 1750 K across a region of 1–3 mm. It is interesting to note that these temperatures are much higher than dark zone temperatures of RDX/GAP/BTTN (1200–1300 K) [3] and HMX/GAP/BTTN (1400–1440 K) [5]. Above 3 mm from the surface, the increase of temperature becomes faster again and reaches 2200 K when approaching the luminous flame at 6 mm above the surface [see Fig. 3c]. The large temperature gradient near the surface region indicates the likelihood of vigorous gas-phase reactions taking place and thus species changes in this reaction zone should be expected.

### Measurement of Species

Experiments to obtain the gaseous species of BTTN/GAP were conducted in argon at 1 atm pressure, because argon helps to eliminate $N_2$ and $O_2$ present in an air background. Under these test conditions, self-sustained combustion of the sample was not achieved, requiring laser heating assistance until completion of combustion. It should be noted that the species data collected under these conditions may not be the same as those collected from self-sustained combustion in air because the laser heating will affect the surface temperature and hence the species near the surface. In future work, experiments are planned to compare the data collected under these different conditions. In the present work, the heat flux was 35 W/cm$^2$ and the sample side surfaces were not coated. Data collection in all tests with species measurements begin about 5 s before the start of heating of the sample by the laser and ends 10 s after the depletion of sample. Unlike pure BTTN [13] or GAP, [19] smoke, suggesting vaporization of the materiel, was not observed during the testing with BTTN/GAP.

Initial mass scans were made over m/z from 1 to 150 amu, and the consistently detected species were distributed within a range of m/z

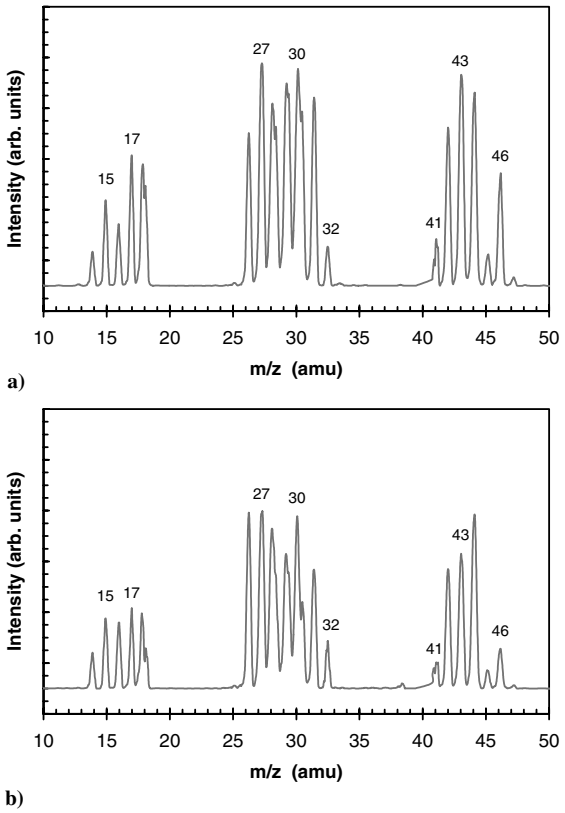


**Fig. 7 Spectra of BTTN/GAP during laser-assisted combustion at 35 W/cm$^2$ in 1 atm argon taken at a) sample surface; b) 2 mm above surface.**

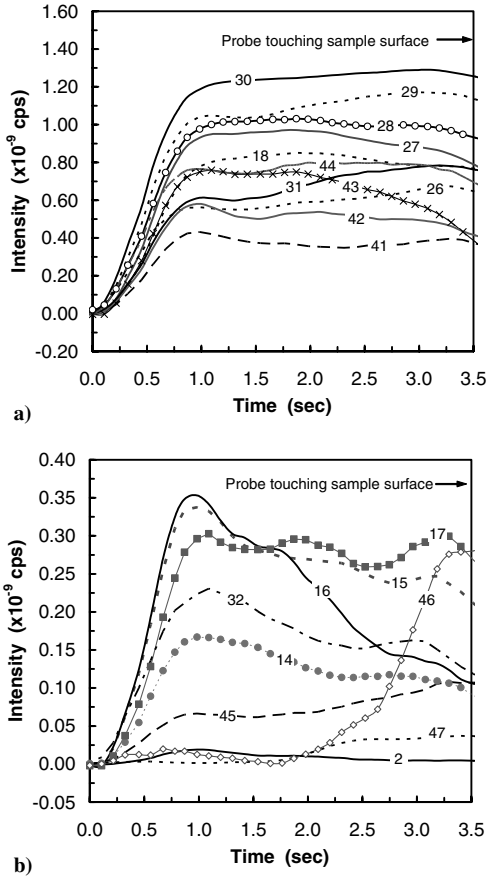


**Fig. 8 Evolution of species of BTTN/GAP in 1 atm argon at 35 W/cm$^2$: a) species with higher intensity; b) species with lower intensity (cps denotes counts per second).**

at 2–47 amu; no peaks at m/z higher than 47 amu were observed in the current study. Figure 7 presents a typical result of mass spectra taken at the sample surface and 2 mm above the surface. The background has been subtracted from the spectra and the part with m/z smaller than 10 amu was omitted for a better presentation for the major species.

As one can see in Fig. 7, distribution of the species was focused on three ranges including m/z at 14–18, 26–32, and 41–47 amu. It should be noted that m/z 2 was also present but with small intensity in the near-surface region. Comparison of the two spectra reveals varying intensities of species at the surface and in the flame, especially the peak at m/z 46, which will be further discussed later.

Figure 8 presents temporal species profiles to give a whole picture of how these species evolve with time. To profile the species across a region from the sample surface to a certain distance above the surface, the regression rate of the sample was measured in separate tests, typically 1.5–1.7 mm/s in the argon environment. Before the test, a sample of 8 mm (height) was placed 3 mm under the probe tip, and the linear positioner was programmed to move up towards the probe at a speed of 2.5 mm/s. Under these conditions, after the sample is ignited, it takes about 3–4 s for the probe tip to touch the sample surface before the combustion is over. As shown in Fig. 8, the probe touched the sample surface at about 3.5 s in this test.

Assignment of these peaks to particular species is straightforward for some species, for instance, m/z 18 is $H_2O$ and 32 is $O_2$, but needs additional experiments with daughter mode operation of the TQMS to identify and differentiate signals that have multiple possibilities of species, such as m/z at 28, 30, 44, etc.

### Identification and Differentiation of Species

The TQMS was run in daughter mode to differentiate species that have the same molecular weight, and the result was summarized in Table 1. Most of the parent species were identified through analysis of their corresponding daughter ions by comparison with standard daughters from calibration tests. However, a few assignments remain tentative due to the lack of standard daughter spectra.

Since the electron energy supplied to the ionizer was not high (22 eV), which is not likely to produce double-charged species in the current study, the mass to charge ratio of each ion is assumed to equal the molecular weight of its corresponding molecule. Based on this assumption, m/z 44 has three candidates for the parent species, $CO_2$, $N_2O$, and $CH_3CHO$. Compared with the standard daughters of these parents, the daughter ions at m/z 28 and 16 indicate the presence of $CO_2$; m/z 30 is from $N_2O$; m/z at 29 and 15 can only come from $CH_3CHO$. Therefore, all these three species are contributing to m/z 44. However, $CO_2$ dominates in the signals because the intensities of its daughter ions are much higher than those of the daughters from the other two parent species.

The signal at m/z 43 may also contain multiple species. Roos and Brill [13] observed a small signal of HNCO from flash pyrolysis of BTTN, so that it is likely that the species at m/z 43 include HNCO. However, the daughter ions cannot be explained solely by HNCO; for example, the daughter ion at 41 must come from species other than HNCO. Tang et al. [19] studied GAP using a TQMS and stated that m/z 43 could be $CH_3CHNH$ and $CH_3CHO$ with the latter being a fragment of $CH_3CHO$ at m/z 44. $CH_3CHNH$ and $CH_3CHO$ well interpret the daughter ions, so that they together with HNCO should account for m/z 43.

Species at m/z 42 has been reported as $CH_2CO$ from thermal decomposition of GAP [18] and BTTN/GAP [4], but $CH_2CO$ cannot produce the daughters at m/z 15 or 27 observed in the current study. The radical $CH_3CHNH$, as a fragment ion from $CH_3CHNH$ formed in the ionizer, provides a possible match to the observed daughters. The peak at m/z 41 is believed to be acetonitrile ($CH_3CN$), because it can have all the detected daughter ions. Also, $CH_3CN$ was found in the mass spectrometric studies of GAP combustion from both Korobeinichev et al. [21] and Tang et al. [19]. The parent species at m/z 31 could be HNO or $CH_3NH_2$, or both, because they can be

**Table 1 Identification and differentiation of species by daughter ions**

| m/z | Daughter ions[a] | Probable parents | Notes |
|---|---|---|---|
| 44 | 28 > 16 ≫ 29 > 15, 12, 14, 30 | $CO_2$, $CH_3CHO$, $N_2O$ | |
| 43 | 15 ≫ 14, 14, 28, 16, 27, 13, 42, 41, 12 | HNCO, $CH_3CHNH$, $CH_3CO$ | $CH_3CO$: fragment of $CH_3CHO$ |
| 42 | 15 > 14, 41, 27, 26, 28, 13 | $CH_2CO$, $CH_3CHN$ | $CH_3CHN$: fragment of $CH_3CHNH$ |
| 41 | 15 > 14, 40, 39, 26, 13, 27 | $CH_3CN$ | |
| 31 | 30 > 16 > 14, 15 | HNO, $CH_3NH_2$ | |
| 30 | 29 ≫ 14 > 16 > 28 ≫ 13 | $CH_2O$, NO | |
| 29 | 28 ≫ 13, 12, 27, 14, 26, 16 | CHO, $CH_2NH$ | CHO: fragment of $CH_2O$ |
| 28 | 27, 14, 12, 26 ≫ 25, 13, 16 | $C_2H_4$, CO, $N_2$ | |
| 27 | 26 ≫ 25, 12, 13, 14 > 15 | HCN, $C_2H_3$ | $C_2H_3$: fragment of $C_2H_4$ |
| 26 | 25 ≫ 12, 13, 24, 14 | $C_2H_2$ | |

[a]Daughter ions listed in a descending order of signal intensity at sample surface.

**Table 2 Comparison of detectable species from thermal decomposition and combustion of BTTN, GAP, and BTTN/GAP from different studies**

| m/z | BTTN | | GAP | | BTTN/GAP | |
|---|---|---|---|---|---|---|
| | Roos and Brill [13][a] | Parr and Hanson-Parr. [11][b] | Arisawa and Brill [18][c] | Tang et al. [19][d] | Roos and Brill [4][e] | Current study |
| 47 | | | | | | |
| 46 | $NO_2$ | | | | | |
| 45 | | | | | | |
| 44 | $CO_2$, $N_2O$ | $CO_2$, $N_2O$ | | $CH_3CHO$ | $CO_2$, $N_2O$ | $CO_2$, $CH_3CHO$, $N_2O$ |
| 43 | HNCO | | | $CH_3CHNH$ | | HNCO, $CH_3CHNH$ |
| 42 | | | $CH_2CO$ | | $CH_2CO$ | $CH_2CO$ |
| 41 | | | | $CH_3CN$, $CH_2NH$ | | $CH_3CN$ |
| 32 | $O_2$ | $O_2$ | | | | $O_2$ |
| 31 | | | | | | HNO, $CH_3NH_2$ |
| 30 | $CH_2O$, NO | $CH_2O$, NO | $CH_2O$ | $CH_2O$ | $CH_2O$, NO | $CH_2O$, NO |
| 29 | | | | $CH_2NH$ | | |
| 28 | CO, $C_2H_4$, $N_2$ | CO, $C_2H_4$, $N_2$ | CO, $C_2H_4$, $N_2$ | CO, $C_2H_4$, $N_2$ | CO, $C_2H_4$, $N_2$ | CO, $C_2H_4$, $N_2$ |
| 27 | HCN | HCN | HCN | HCN | HCN | HCN |
| 26 | $C_2H_2$ | $C_2H_2$ | | | $C_2H_2$ | $C_2H_2$ |
| 18 | $H_2O$ | $H_2O$ | $H_2O$ | $H_2O$ | $H_2O$ | $H_2O$ |
| 17 | | | $NH_3$ | $NH_3$ | $NH_3$ | $NH_3$ |
| 16 | $CH_4$ | $CH_4$ | $CH_4$ | $CH_4$ | $CH_4$ | $CH_4$ |
| 15 | | | | | | $CH_3$ |
| 14 | | | | | | $CH_2$ |
| 2 | $H_2$ | $H_2$ | | | $H_2$ | $H_2$ |

[a]Flash pyrolysis, 5 atm argon, 2000°C/s to 400°C.
[b]Self-sustained combustion, 1 atm air.
[c]Uncured GAP polyol, flash pyrolysis, 2 atm argon, 800 K/s to 500–600 K.
[d]Cured GAP polyol, laser-assisted combustion, 1 atm argon, 50–200 W/cm$^2$ (also found species at 54–57).
[e]Cured 70/30 BTTN/GAP polyol, flash pyrolysis, 5 atm argon 2000°C/s to 450°C.

interpreted by the measured daughters. A more concrete assignment of species is not possible due to the lack of standard daughter spectra for these species.

Species at m/z 30 was found to include both $CH_2O$ and NO based on their standard daughters: m/z 29, 14, 28, 13 for $CH_2O$, and 14, 16 for NO. Species at m/z 29 must include CHO, a fragment of $CH_2O$, because of a good match of its daughters at m/z 28, 13 and 12 with the standards. However, the daughter ions at m/z 27, 14, 26 and 16 indicate that other species are also contributing to the signal at m/z 29. Tang et al. [19] suggested that it was $CH_2NH$ from GAP.

Species at m/z 28 are believed to include $C_2H_4$, CO and $N_2$, because the daughter ions match well with the standards, where $C_2H_4$, is characterized by daughters at m/z 27, 26 and 25; CO by 12 and 16; $N_2$ by 14. Results from other researchers [4,11,13,18,19] all supported this claim. Species at m/z 27 are HCN and $C_2H_3$, with the latter being indicated exclusively by the daughter ion m/z 25 and likely a fragment from $C_2H_4$ or even larger hydrocarbons. Species at m/z 26 is $C_2H_2$ as identified by its daughters.

To compare the species of BTTN, GAP, and BTTN/GAP from other researchers with the current study, a summary was made in Table 2, where all the detectable species from both thermal decomposition and combustion of these binders are listed. The thermal decomposition studies were performed during flash pyrolysis at high heating rates, and the combustion studies were conducted with laser heating support. As seen from the table, most of the species measured in the current study were commonly observed from the experimental studies of BTTN or GAP, but there are several species that were never reported, which is likely due to the different test conditions used in other studies.

Species at m/z 47 was proposed by the modelers [2] to be a decomposition product of BTTN, which has a structure of H–O–N = O. However, as shown in Table 2, previous researchers made no mention of it, probably because of its small concentration. The peaks at m/z 31 and 45 are two other species not mentioned. The m/z 31 could be HNO or $CH_3NH_2$, and was reasonably abundant in the products; whereas m/z 45 was tentatively proposed to be $C_2H_4OH$, a fragment of $CH_3CH_2OH$ (ethyl alcohol), which needs further experiment to verify. The radicals of $CH_3$ and $CH_2$ were fragments from $CH_4$ and $C_2H_4$ due to electron impact in the ionizer.

### Quantitative Species Profile

Sensitivity coefficients were obtained from calibration tests for most of the species that are readily available. Estimation was made for the remaining species based on a close match in their ionization cross sections with that of species having calibration data. Also, analysis of the element balance was performed to help determine the mole fractions of those species for which standard calibration data were not available. Some species were omitted due to their really small signal intensity, such as $CH_3NH_2$, $CH_3CHO$, and $CH_2NH$. Since not all the species were taken into account due to difficulty in

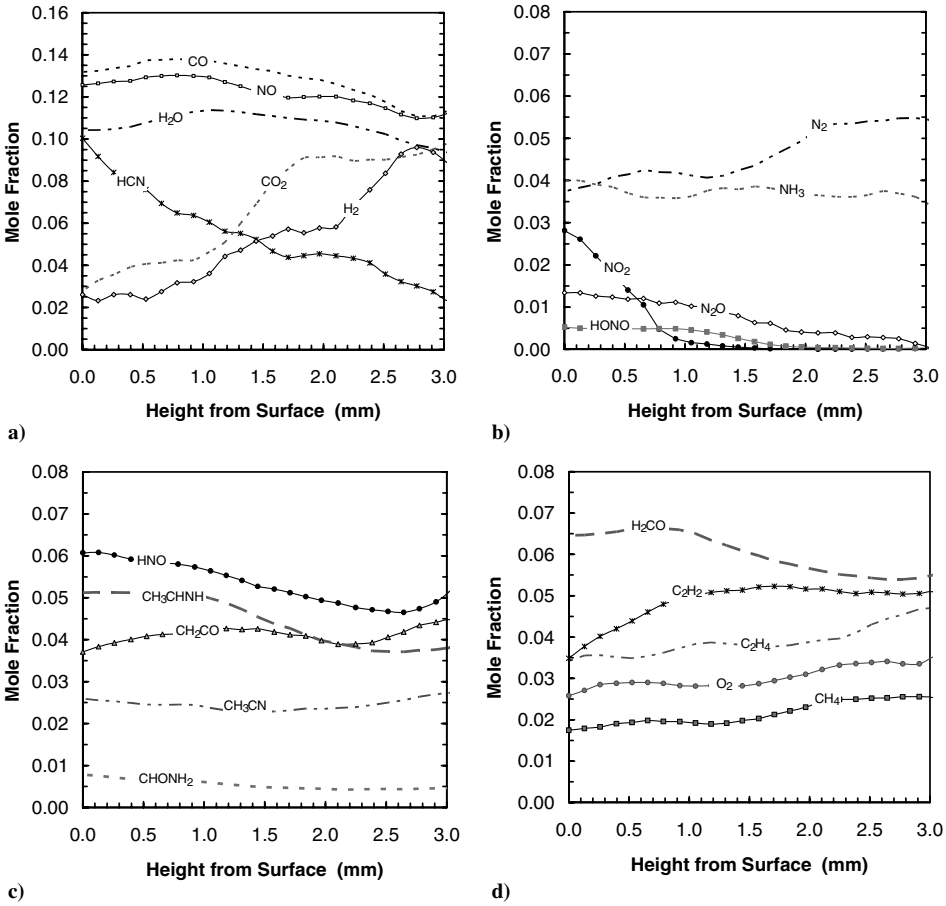


**Fig. 9 Quantitative species profiles near the surface of BTTN/GAP during laser-assisted combustion at 35 W/cm$^2$ in 1 atm argon.**

quantitative differentiation, precise element balances may not be expected.

Figure 9 presents a typical test result for species profiles. In the plots, the zero height corresponds to the point where the sampling probe touched the sample surface, which was determined by the initial probe-to-sample distance, and by the burning rate as well as the speed of the linear positioner. The moment for the probe touching the surface was also confirmed by closely observing the video of the test. The profiles for all considered species were separately plotted and displayed in the figure as a), b), c) and d). It is noted that the scale for *y* axis (mole fraction) in Figs. 9b–9d was enlarged in order to better show species variations across the near-surface region.

Across a region of 3 mm above the surface, significant changes in mole fraction were found for species $NO_2$, $N_2O$, HCN, $CO_2$, $H_2$, $N_2$, and HONO, and all others change fairly slowly. $NO_2$ is the most rapidly changing species, and only present within about 1.0 mm above the surface; beyond 1.0 mm, it was consumed. HONO remained inert though this region, but was also consumed beyond about 2.0 mm from the surface. HCN, which also changed rapidly within 1.0 mm, is being consumed. $CO_2$, $H_2$, and $N_2$ all rise, but $N_2O$ drops, as the distance from surface became larger.

The major species appeared to be CO, NO, and $H_2O$ in the near-surface region; this is consistent with the BTTN combustion result from Parr and Hanson-Parr [11], who measured mole fractions of 30%, 26%, and 20.7% for CO, NO, and $H_2O$, respectively. However, the pyrolysis of BTTN/GAP from Roos and Brill [4] measured a much smaller $H_2O$ (0.234 moles), but CO and NO were also large, 1.675 moles and 1.127 moles, respectively. This discrepancy should be attributed to the different conditions of the rapid pyrolysis from the combustion test.

Arisawa and Brill [18] stated that the initial decomposition of GAP may start with a simultaneous H shift and breaking of the $RCH_2N = N_2$ bond to form an imine ($RCH = NH$) and $N_2$. However, Kubota and Sonobe [15] suggested that the initial step leading to decomposition of GAP involve the scission of $N_2$ from the azide to form a nitrene ($RC \equiv N$), $H_2$, and $N_2$. From the current study, it seems that both reactions could simultaneously take place judged by the relatively abundant $H_2$ and $N_2$ near the surface and the appearance of the nitrene $CH_3CN$ and the imines $CH_2NH$ and $CH_3CHNH$.

Lin at Emory University proposed three decomposition pathways for BTTN, as illustrated in Fig. 10. The measured near-surface species $NO_2$, HONO, and $CH_2O$ seem to confirm their mechanism. The species, ethylene oxide ($H_2COCH_2$), could isomerize to give $CH_3CHO$, because the latter was more likely to be a product that accounts for the daughter ions at m/z 15, 29 of m/z 44 (see Table 1)

Element balance was calculated to check how large the error would be in the results obtained, and the typical result is presented in Fig. 11. All elements that were in the starting material should be in the flame species and therefore should be considered. For the tested material, BTTN/GAP, the mole fraction of the element C is 0.182, H 0.356, N 0.153, and O 0.309. As shown in Fig. 11, the consistency of the data with element balance is fairly good. The mole fractions measured averaged over the 0–3 mm region are 0.192 (C), 0.341 (H), 0.164 (N), and 0.293 (O). Larger variations were found near the surface, which may be due to the omitted species or may indicate that some species were not detected. Another possibility that could account for the discrepancy is the loss of mass due to the popping bright sparks as observed in the video images shown in Fig. 3. Also, the estimated sensitivity coefficients for some species could have an impact on the element balance calculations.

## Summary and Conclusion

The gas-phase quantitative species from $CO_2$ laser-induced decomposition and laser-assisted combustion of BTTN/GAP was studied using a triple quadrupole mass spectrometer. To get the species profile, a linear positioner was used to move the sample towards the microprobe during sampling. Fine-wire thermocouples

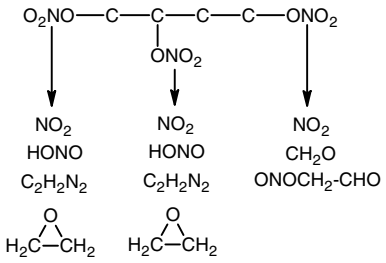


**Fig. 10 Decomposition pathways of BTTN.**

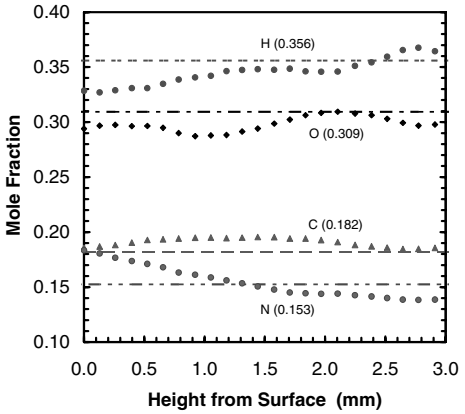


**Fig. 11 Species element fractions near the surface of BTTN/GAP during laser-assisted combustion at 35 $W/cm^2$ in 1 atm argon.**

were used to get the surface temperature and gas-phase temperature profile in the primary flame zone. The experiments were conducted at a laser heat flux of 35 $W/cm^2$ and in both argon environment and ambient air conditions with varying pressures from 1.0 to 4.0 atm. The flame structure and burning event were recorded using a digital camcorder to determine the burning rates at these pressures.

The results showed that, in atmospheric air, the surface temperature of BTTN/GAP was $510 \pm 6$ K. The temperature rises rapidly to $\sim$1650 K within a distance of about 1 mm from the surface, and then the increase becomes gradually from 1650 to 1750 K across a region of 1–3 mm, which is much higher than the dark zone temperatures of RDX/GAP/BTTN (1200–1300 K) and HMX/GAP/BTTN (1400–1440 K). Over a pressure range of 0.1 to 0.4 MPa, the increase in surface temperature at a higher pressure was not large, only about 10 K as pressure increases from 0.1 to 0.4 MPa. At these low pressures, the burning rate increases almost linearly from $\sim$0.5 mm/s to $\sim$1.4 mm/s with pressure. The consistently detected species were distributed within a range of $m/z$ 2–47 amu; no signals at $m/z$ higher than 47 amu were observed in the current study. The observed species were identified to include $H_2$, $CH_4$, $NH_3$, $H_2O$, $C_2H_2$, HCN, $N_2$, CO, $C_2H_4$, $CH_2NH$, NO, $CH_2O$, HNO, $CH_3NH_2$, $O_2$, $CH_3CN$, $CH_2CO$, $CH_3CHNH$, $CO_2$, $CH_3CHO$, $N_2O$, $C_2H_4OH$, $NO_2$, and HONO. Among these, CO, NO, and $H_2O$ appear to be the major species; $NO_2$ and HONO are only present within about 1.5 mm from the surface.

It is hoped that these results from the current study will help modelers to deduce the mechanisms occurring above the burning surface of the material and to probe likely condensed-phase processes occurring in the BTTN/GAP material during combustion.

## Acknowledgments

This work was funded by a subcontract from SEA, Carson City, Nevada, who was funded by U.S. Office of Naval Research Contract N00014-02-C-0292, Judah Goldwasser as Contract Monitor. The authors wish to thank Tim Parr of the U.S. Naval Air Warfare Center for providing the BTTN/GAP material.

## References

[1] Beckstead, M. W., and Puduppakkam, K., "Modeling and Simulation of Combustion of Solid Propellant Ingredients Using Detailed Chemical Kinetics," AIAA Paper 2004-4036, 2004.

[2] Puduppakkam, K. V., and Beckstead, M. W., "Combustion Modeling of RDX/GAP/BTTN Pseudo-Propellant," *Combustion Science and Technology* Vol. 177, No. 9, 2005, pp. 1661–1697.

[3] Parr, T., and Hanson-Parr, D., "RDX/GAP/BTTN Propellant Flame Studies," *Combustion and Flame*, Vol. 127, No. 1–2, 2001, pp. 1895–1905.

[4] Roos, B. D., and Brill, T. B., "Thermal Decomposition of Energetic Material 81: Flash Pyrolysis of GAP/RDX/BTTN Propellant Combinations," *Propellants, Explosives, Pyrotechnics*, Vol. 26, No. 5, 2001, pp. 213–220.

[5] Parr, T., and Hanson-Parr, D., "Cyclotetramethylene Tetranitramine/Glycidyl Azide Polymer/Butanetriol Trinitrate Propellant Flame Structure," *Combustion and Flame*, Vol. 137, No. 1–2, 2004, pp. 38–49.

[6] Lee, Y., Tang, C.-J., and Litzinger, T. A., "A Study of the Chemical and Physical Processes Governing $CO_2$ Laser-Induced Pyrolysis and Combustion of RDX," *Combustion and Flame*, Vol. 117, No. 3, 1999, pp. 600–628.

[7] Litzinger, T. A., Fetherolf, B. L., Lee, Y., and Tang, C.-J., "Study of the Gas-Phase Chemistry of RDX: Experiments and Modeling," *Journal of Propulsion and Power*, Vol. 11, No. 4, 1995, pp. 698–703.

[8] Zenin, A., "HMX and RDX: Combustion Mechanism and Influence on Modern Double-Base Propellant Combustion," *Journal of Propulsion and Power*, Vol. 11, No. 4, 1995, pp. 752–758.

[9] Behrens, R., "Thermal Decomposition of Energetic Materials. Temporal Behaviors of the Rates of Formation of the Gaseous Pyrolysis Products of HMX," *Journal of Physical Chemistry*, Vol. 94, No. 7, 1990, pp. 6706–6718.

[10] Tang, C.-J., Lee, Y., and Litzinger, T. A., "Simultaneous Temperature and Species Measurements During Self-Oscillating Burning of HMX," *Journal of Propulsion and Power*, Vol. 15, No. 2, 1999, pp. 296–303.

[11] Parr, T., and Hanson-Parr, D., "BTTN Flame Structure," *Proceedings of the 38th JANNAF Combustion Subcommittee Meeting*, Vol. 1, Johns Hopkins University, Baltimore, MD, 2002, pp. 43–49; Chemical Propulsion Information Agency Publication 712.

[12] Oyumi, Y., and Brill, T. B., "Thermal Decomposition of Energetic Materials 14. Selective Product Distributions Evidenced in Rapid, Real-Time Thermolysis of Nitrate Esters at Various Pressures," *Combustion and Flame*, Vol. 66, No. 1, 1986, pp. 9–16.

[13] Roos, B. D., and Brill, T. B., "Thermal Decomposition of Energetic Material 82. Correlations of Gaseous Products with the Composition of Aliphatic Nitrate Esters," *Combustion and Flame*, Vol. 128, No. 1–2, 2002, pp. 181–190.

[14] Farber, M., Harris, S. P., and Srivastava, R. D., "M/z Spectrometric Kinetic Studies on Several Azido Polymers," *Combustion and Flame*, Vol. 55, No. 2, 1984, pp. 203–211.

[15] Kubota, N., and Sonobe, T., "Combustion Mechanism of Azide Polymer," *Propellants, Explosives, Pyrotechnics*, Vol. 13, No. 6, 1988, pp. 172–177.

[16] Chen, J. K., and Brill, T. A., "Thermal Decomposition of Energetic Materials 54. Kinetics and Near-Surface Products of Azide Polymers AMMO, BAMO, and GAP in Simulated Combustion," *Combustion and Flame*, Vol. 87, No. 2, 1991, pp. 157–168.

[17] Haas, Y., Ben-Eliahu, Y., and Welner, S., "Infrared Laser-Induced Decomposition of GAP," *Combustion and Flame*, Vol. 96, No. 3, 1994, pp. 212–220.

[18] Arisawa, H., and Brill, T. B., "Thermal Decomposition of Energetic Materials 71: Structure-Decomposition and Kinetic Relationships in Flash Pyrolysis of Glycidyl Azide Polymer (GAP)," *Combustion and Flame*, Vol. 112, No. 4, 1998, pp. 533–544.

[19] Tang, C.-J., Lee, Y., and Litzinger, T. A., "Simultaneous Temperature and Species Measurements of the Glycidyl Azide Polymer (GAP) Propellant During Laser-Induced Decomposition," *Combustion and Flame*, Vol. 117, No. 1–2, 1999, pp. 244–256.

[20] Saito, T., Shimoda, M., Tsuyuki, T., and Iwama, A., "$CO_2$ Laser-Induced Pulsating Regresson Behavior of GAP at Sub-Atmospheric Pressures," *Combustion and Flame*, Vol. 124, No. 4, 2001, pp. 611–623.

[21] Korobeinichev, O. P., Kuibida, L. V., Volkov, E. N., and Shmakov, A. G., "M/z Spectrometric Study of Combustion and Thermal Decomposition of GAP," *Combustion and Flame*, Vol. 129, No. 1–2, 2002, pp. 136–150.

[22] Jakob, M., *Heat Transfer*, Vol. 2, John Wiley & Sons, Inc., New York, NY, 1959, p. 151.

[23] Fetherolf, B. L., "The Physical and Chemical Processes Governing $CO_2$ Laser-Induced Pyrolysis and Combustion of the Solid Propellants RDX, AND, XM39, and M43," Ph.D. Dissertation, Mechanical and Nuclear Engineering Department, Pennsylvania State University, 1993.

[24] Lee, Y., Tang, C.-J., and Litzinger, T. A., "Triple Quadrupole M/z Spectrometer System for Studies of Gas-Phase Combustion Chemistry of Energetic Materials," *Measurement Science and Technology*, Vol. 9, No. 9, 1998, pp. 1576–1586.

[25] Li, J.-Q., "A Study of an Electrothermal Plasma and its Interaction with Propellants," Ph.D. Dissertation, Mechanical and Nuclear Engineering Department, Pennsylvania State University, 2004.

[26] Lee, Y., Tang, C.-J., and Litzinger, T. A., "A Study of the Chemical and Physical Processes Governing $CO_2$ Laser-Induced Pyrolysis and Combustion of RDX," *Combustion and Flame*, Vol. 117, No. 3, 1999, pp. 600–628.

[27] Schoenung, S. M., and Hanson, R. K., "CO and Temperature Measurements in a Flat Flame by Laser Absorption Spectroscopy and Probe Techniques," *Combustion Science and Technology*, Vol. 24, 1981, pp. 227–237.

[28] Kramlich, J. C., and Malte, P. C., "Modeling and Measurement of Sample Probe Effects on Pollutant Gases Drawn from Flame Zones," *Combustion Science and Technology*, Vol. 18, 1978, pp. 91–104.

[29] Bobeldijk, M., Van der Zande, W. J., and Kistemaker, P. G., "Simple Models for the Calculation of Photoionization and Electron Impact Ionization Cross-Sections of Polyatomic Molecules," *Chemical Physics*, Vol. 179, No. 2, 1994, pp. 125–130.

S. Son
*Associate Editor*